A phase-cycled temperature-sensitive fast spin echo sequence with conductivity bias correction for monitoring of mild RF hyperthermia with PRFS

Citation for published version (APA):
Wu, M., Mulder, H. T., Zur, Y., Lechner-Greite, S., Menzel, M. I., Paulides, M. M., van Rhoon, G. C., & Haase, A. (2019). A phase-cycled temperature-sensitive fast spin echo sequence with conductivity bias correction for monitoring of mild RF hyperthermia with PRFS. *Magnetic Resonance Materials in Physics, Biology and Medicine*, *32*(3), 369-380. https://doi.org/10.1007/s10334-018-0725-5

Document license:
TAVERNE

DOI:
10.1007/s10334-018-0725-5

Document status and date:
Published: 01/06/2019

Document Version:
Publisher's PDF, also known as Version of Record (includes final page, issue and volume numbers)

Please check the document version of this publication:

• A submitted manuscript is the version of the article upon submission and before peer-review. There can be important differences between the submitted version and the official published version of record. People interested in the research are advised to contact the author for the final version of the publication, or visit the DOI to the publisher's website.
• The final author version and the galley proof are versions of the publication after peer review.
• The final published version features the final layout of the paper including the volume, issue and page numbers.

Link to publication

General rights
Copyright and moral rights for the publications made accessible in the public portal are retained by the authors and/or other copyright owners and it is a condition of accessing publications that users recognise and abide by the legal requirements associated with these rights.

- Users may download and print one copy of any publication from the public portal for the purpose of private study or research.
- You may not further distribute the material or use it for any profit-making activity or commercial gain
- You may freely distribute the URL identifying the publication in the public portal.

If the publication is distributed under the terms of Article 25fa of the Dutch Copyright Act, indicated by the "Taverne" license above, please follow below link for the End User Agreement:

www.tue.nl/taverne

Take down policy
If you believe that this document breaches copyright please contact us at:

openaccess@tue.nl

providing details and we will investigate your claim.

Download date: 04. Oct. 2023

Magnetic Resonance Materials in Physics, Biology and Medicine (2019) 32:369–380
https://doi.org/10.1007/s10334-018-0725-5

RESEARCH ARTICLE

A phase-cycled temperature-sensitive fast spin echo sequence with conductivity bias correction for monitoring of mild RF hyperthermia with PRFS

Mingming Wu[1] · **Hendrik T. Mulder**[2] · **Yuval Zur**[3] · **Silke Lechner-Greite**[4] · **Marion I. Menzel**[4] · **Margarethus M. Paulides**[2] · **Gerard C. van Rhoon**[2] · **Axel Haase**[1]

Received: 5 June 2018 / Revised: 21 November 2018 / Accepted: 22 November 2018 / Published online: 4 December 2018

Abstract

Objective Mild hyperthermia (HT) treatments are generally monitored by phase-referenced proton resonance frequency shift calculations. A novel phase and thus temperature-sensitive fast spin echo (TFSE) sequence is introduced and compared to the double echo gradient echo (DEGRE) sequence.

Theory and methods For a proton resonance frequency shift (PRFS)-sensitive TFSE sequence, a phase cycling method is applied to separate even from odd echoes. This method compensates for conductivity change-induced bias in temperature mapping as does the DEGRE sequence. Both sequences were alternately applied during a phantom heating experiment using the clinical setup for deep radio frequency HT (RF-HT). The B_0 drift-corrected temperature values in a region of interest around temperature probes are compared to the temperature probe data and further evaluated in Bland–Altman plots. The stability of both methods was also tested within the thighs of three volunteers at a constant temperature using the subcutaneous fat layer for B_0-drift correction.

Results During the phantom heating experiment, on average TFSE temperature maps achieved double temperature-to-noise ratio (TNR) efficiency in comparison with DEGRE temperature maps. In-vivo images of the thighs exhibit stable temperature readings of ± 1 °C over 25 min of scanning in three volunteers for both methods. On average, the TNR efficiency improved by around 25% for in vivo data.

Conclusion A novel TFSE method has been adapted to monitor temperature during mild HT.

Keywords MR thermometry · Hyperthermia · Proton resonance frequency shift · Fast spin echo · Double echo gradient echo · Intervention · Conductivity

Introduction

Mild hyperthermia (HT) (40–44 °C) sensitizes tumor cells to radio- and chemotherapy and is therefore applied as a complementary treatment for various types of cancer [1]. Temperature monitoring during treatment is necessary to ensure sufficient thermal exposure in the target region and to prevent critical structures from overheating. Temperature monitoring with invasive probes is very accurate, but provides limited spatial information on the temperature distribution. In addition, side effects such as local inflammation, pain, or abscess formation, may be caused [2, 3]. MR thermometry circumvents these limitations and complications by measuring the temperature non-invasively across a large volume with a high spatial resolution. MR thermometry also plays a decisive role even prior to patient heating: simulated treatment planning is validated using generic human tissue mimicking phantoms during MR-monitored electromagnetic radio frequency (RF) heating experiments [4].

The most widespread method for MR-based temperature monitoring is based on the linear proton resonance frequency shift (PRFS) of protons in water molecules with temperature

✉ Mingming Wu
mingming.wu@tum.de

[1] Munich School of Bioengineering, Technical University of Munich, Boltzmannstr. 11, 85748 Garching bei München, Germany

[2] Erasmus MC Cancer Institute, Rotterdam, The Netherlands

[3] GE Healthcare, Haifa, Israel

[4] GE Healthcare, Munich, Germany

[5]. By calculating the phase difference between a gradient echo (GRE) image at a certain temperature and a reference temperature, the temperature change can be deduced [6].

The Double Echo GRE (DEGRE), also known as Dual-Echo GRE, has commonly been used in the clinical practice of regional mild RF-HT [7, 8] with the advantage that it is able to eliminate the bias with temperature-induced conductivity changes [9]. Since the heated area during mild RF-HT is not locally confined, the bias cannot be neglected.

For the mild RF-HT treatment of deeply located cancers in the pelvis and leg, generally the constructive interference of coherent RF waves from multiple antennas is applied to achieve heating of the tumor. Since there is no additional space for a dedicated MR receiving coil [10], the body coil is used for MR signal transmission and receiving. This leads to low signal-to-noise ratio (SNR) values in the MR images [11, 12] and, since phase noise is inversely proportional to SNR [13], to a low temperature-to-noise ratio (TNR). As a tight optimum temperature range must be achieved during mild HT, temperature accuracy and precision are of great importance. In addition, a low phase precision hampers the disentangling of temperature- and non-temperature induced phase confounders and leads to errors in the temperature reading [14].

The TNR could be improved by changing the imaging sequence from GRE to a fast spin echo (FSE) readout [15]. By introducing a variable waiting time between the excitation pulse and the train of refocusing pulses, the phase of the FSE image becomes sensitive to chemical shift. This initial phase value accumulated during a waiting time corresponds to the accumulated phase at TE in a GRE sequence. It can be obtained from the successive overlapping echoes in different ways: in one approach, the carrier phase of the refocusing pulses is modulated [16]. In another approach, the gradients are manipulated so that an asymmetric readout allows for a splitting of the pure spin echo and stimulated echoes in time [17, 18]. Selective parity imaging, meaning selective even and odd echo imaging, has also been achieved with asymmetric readout gradients [19]. However, the methods referred to do not correct for the phase bias introduced by conductivity change with temperature. Here, we use a phase cycling approach first demonstrated by [20], which acquires the same *k*-space once under a Carr–Purcell (CP) condition and another time under a Carr–Purcell–Meiboom–Gill (CPMG) condition [21–23] to split the even and odd echoes and correct for the confounding background phase. This technique had been applied to eliminate artifacts in 3D FSE imaging [24]. A detailed analytical explanation of this method is given in [25]. It has also been successfully implemented to extract temperature changes from the phase changes due to PRFS [26] during high-intensity focused ultrasound (HIFU) experiments. Via phase-cycling, a background phase correction is realized, eliminating all effects from eddy currents and conductivity change-induced temperature errors [9].

The main magnetic field drifts over time due to various hardware instabilities or gradient coil-heating during scanning [27]. This field drift causes additional phase changes that would be falsely interpreted as a temperature change. A robust B_0-drift correction is crucial for mild HT applications, because the temperature bias due to drift is of the order of the expected temperature increase [28]. Here, the drift was calculated using a 3D polynomial fit based on the signal within reference areas and then subtracted from the measured phase [29].

In this work, we exploit this novel temperature-sensitive fast spin echo (TFSE) sequence to monitor mild RF-HT and compare it to the clinically prevailing DEGRE method in terms of temperature precision and accuracy. We derive the theory of the phase shift calculation and compare the performance of TFSE to DEGRE using a heating experiment on a phantom as well as at constant temperature in three human subjects.

Theory

DEGRE

The double echo GRE (also known as Dual Echo GRE) creates two echoes at different echo times after one slice-selective RF excitation with the frequency-encoding gradient (Fig. 1a). Using the phases at both TEs compensates for conductivity change-induced phase offsets [9]. The temperature increase is obtained via (Eq. 1). The phase difference between long echo time TE_2 and short echo time TE_1 signals at the reference temperature T_{ref} is subtracted from the phase difference between long and short echo time signals at the current temperature T. The multiplication of complex signals instead of direct subtraction of phases prevents small phase changes of about 2π from being misinterpreted. The thermal coefficient α represents the temperature sensitivity of PRFS, γ is the gyromagnetic constant, and B_0 is the main magnetic field strength, $\Delta\mathrm{TE} = \mathrm{TE}_2 – \mathrm{TE}_1$:

$$T - T_{\mathrm{ref}} = \frac{\angle\left(\exp\left(i\phi\left(\mathrm{TE}_2, T\right)\right)\cdot\mathrm{conj}\left(\exp\left(i\phi\left(\mathrm{TE}_1, T\right)\right)\right)\right) - \angle\left(\exp\left(i\phi\left(\mathrm{TE}_2, T_{\mathrm{ref}}\right)\right)\cdot\mathrm{conj}\left(\exp\left(i\phi\left(\mathrm{TE}_1, T_{\mathrm{ref}}\right)\right)\right)\right)}{\alpha\gamma B_0 \Delta\mathrm{TE}}$$

$$= \frac{\angle\left[\exp\left(i\Delta\phi(T)\right)\cdot\mathrm{conj}\left(\exp\left(i\Delta\phi\left(T_{\mathrm{ref}}\right)\right)\right)\right]}{\alpha\gamma B_0 \Delta\mathrm{TE}}. \tag{1}$$

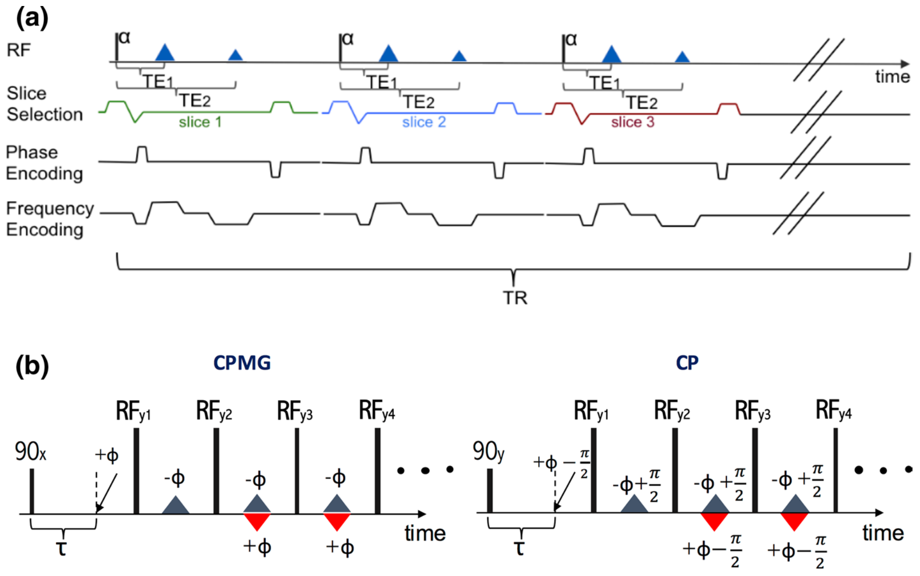

Fig. 1 Sequence diagrams. **a** DEGRE: the frequency-encoding gradient refocuses two echoes within one TR. **b** TFSE: a waiting time τ is inserted between the excitation pulse $90°_x$ about the x-axis (CP) or $90°_y$ about the y-axis (CPMG) and succeeding refocusing pulses RF_{yn} about the y-axis. Even echoes (red triangle) and odd echoes (blue triangles), overlap in time within the acquisition window

TFSE

During a FSE sequence, the excitation pulse RF_0 is followed by a train of refocusing pulses RF_n (Fig. 1b). The measurable signal in each sampling window can be divided into two overlapping echoes with different parities. The even echo has experienced an even number of refocusing pulses, thus an even number of phase inversions. The odd echo has experienced an odd number of refocusing pulses, thus carrying the inverted initial phase. Echoes of higher order, such as stimulated echoes, will also always return to either the phase of an even or odd echo, as demonstrated in [19]. The additional waiting time τ added to the usual time gap of $\frac{1}{2}$TE between 90° RF excitation and first RF refocusing pulse creates a dependency of the image phase on PRF as follows [15]:

$$\phi = 2\pi f_{\mathrm{PRF}}\tau. \tag{2}$$

f_{PRF} represents the proton resonance frequency, that depends on the local B_0 and the temperature. A phase ϕ after τ would shift all even echoes by ϕ and all odd echoes by $-\phi$ (Fig. 1b). However, due to system imperfections, the RF pulses and the received phase have an unknown rotational shift about the z-axis in the x–y plane. The source of the overall resulting phase shift φ_{bg} also includes eddy currents and temperature-dependent conductivity-induced phase offsets.

Splitting even and odd echoes

To separate the superimposed even and odd echo images, we use a phase-cycling approach first demonstrated by [20]. We make use of the known shift of 90° under the CP and the RF pulses under the CPMG condition [21, 22] and thus their orthogonality to split even from odd echoes. The same 2D k-space is acquired twice, the first time under the CP condition and the second time under the CPMG condition [15, 26], which is referred to as phase-cycling. For CPMG, the refocusing pulses following the excitation pulse about the x-axis are rotating about the y-axis (Eq. 4, $RF_{1,2,3,\ldots,y}$ in Fig. 1b). During the CP condition, the refocusing pulses ($RF_{1,2,3,\ldots,x}$ in Fig. 1b) are generally transmitted with regard to the x-axis, just as the initial excitation pulse (Eq. 3). In our approach, we achieve the CP condition by rotating the RF excitation pulse by 90° instead of rotating the refocusing pulses that are kept the same as for CPMG. As mentioned above, a rotational background shift φ_{bg} due to eddy currents and conductivity shifts both CP and CPMG signals in the same direction:

$$\mathrm{Echo}_{\mathrm{CPMG}} = \left[S_1 \cdot \cos\phi + \mathrm{i}S_2 \cdot \sin\phi\right] \cdot \exp\left(\mathrm{i}\varphi_{\mathrm{BG}}\right), \tag{3}$$

$$\begin{aligned}\mathrm{Echo}_{\mathrm{CP}} &= \left[S_1 \cdot \cos(\phi - 90°) + \mathrm{i}S_2 \cdot \sin(\phi - 90°)\right] \cdot \exp\left(\mathrm{i}\varphi_{\mathrm{BG}}\right)\\ &= \left[S_1 \cdot \sin(\phi) - \mathrm{i}S_2 \cdot \cos(\phi)\right] \cdot \exp\left(\mathrm{i}\varphi_{\mathrm{BG}}\right).\end{aligned} \tag{4}$$

S_1 and S_2 are unknown magnetization vectors and ϕ is the refocused phase value. The even echo is calculated by averaging the CPMG image with i times the CP image (Eq. 5). The odd echo is equivalent to half of the difference of both images (Eq. 6) [25].

$$\begin{aligned}E_{\mathrm{even}} &= \frac{\mathrm{Echo}_{\mathrm{CPMG}} + \mathrm{i}\mathrm{Echo}_{\mathrm{CP}}}{2}\\ &= \frac{1}{2}\left[\left(S_1\cos\phi + \mathrm{i}S_2\sin\phi\right.\right.\\ &\quad \left.\left.+\mathrm{i}S_1\sin\phi + S_2\cos\phi\right)\right] \cdot \exp\left(\mathrm{i}\varphi_{\mathrm{BG}}\right)\\ &= \frac{S_1 + S_2}{2}\exp\left(\mathrm{i}\left(\phi + \varphi_{\mathrm{BG}}\right)\right),\end{aligned} \tag{5}$$

$$
\begin{aligned}
E_{\mathrm{odd}} &= \frac{\mathrm{Echo}_{\mathrm{CPMG}} - \mathrm{iEcho}_{\mathrm{CP}}}{2} \\
&= \frac{1}{2}\left[\left(S_1 \cos\phi + \mathrm{i}S_2 \sin\phi \right.\right. \\
&\quad \left.\left. -\mathrm{i}S_1 \sin\phi - S_2 \cos\phi\right)\right] \cdot \exp\left(\mathrm{i}\varphi_{\mathrm{BG}}\right) \\
&= \frac{S_1 - S_2}{2} \exp\left(-\mathrm{i}\left(\phi - \varphi_{\mathrm{BG}}\right)\right).
\end{aligned}
\tag{6}
$$

Extracting PRFS with TFSE

We denote the phase at even and odd echo images at the reference temperature (T_{ref}) as φ_{e1} and φ_{o1}, respectively.

$$
\begin{aligned}
E_{\mathrm{even}}\left(T_{\mathrm{ref}}\right) &= \left|E_{\mathrm{even}}\left(T_{\mathrm{ref}}\right)\right| \cdot \exp\left(\mathrm{i}\left(\phi + \varphi_{\mathrm{BG}}\left(T_{\mathrm{ref}}\right)\right)\right) \\
&= \left|E_{\mathrm{even}}\left(T_{\mathrm{ref}}\right)\right| \cdot \exp\left(\mathrm{i}\phi_{\mathrm{e1}}\right) \\
E_{\mathrm{odd}}\left(T_{\mathrm{ref}}\right) &= \left|E_{\mathrm{odd}}\left(T_{\mathrm{ref}}\right)\right| \cdot \exp\left(-\mathrm{i}\left(\phi - \varphi_{\mathrm{BG}}\left(T_{\mathrm{ref}}\right)\right)\right) \\
&= \left|E_{\mathrm{odd}}\left(T_{\mathrm{ref}}\right)\right| \cdot \exp\left(\mathrm{i}\phi_{\mathrm{o1}}\right).
\end{aligned}
\tag{7}
$$

After a temperature change or field shift-induced PRFS, the even and odd images have experienced a phase shift of $2\pi\Delta f_{\mathrm{PRF}}\tau$. Since the contribution of the different tissue conductivity on the background phase is also temperature-dependent, an additional phase shift in the same direction for even and odd echo needs to be considered.

$$
\begin{aligned}
E_{\mathrm{even}}(T) &= \left|E_{\mathrm{even}}(T)\right| \cdot \exp\left(\mathrm{i}\left(\phi_{\mathrm{e1}} + 2\pi\Delta f_{\mathrm{PRF}}\tau + \Delta\varphi_{\mathrm{BG}}(T)\right)\right) \\
E_{\mathrm{odd}}(T) &= \left|E_{\mathrm{odd}}(T)\right| \cdot \exp\left(\mathrm{i}\left(\phi_{\mathrm{o1}} - 2\pi\Delta f_{\mathrm{PRF}}\tau + \Delta\varphi_{\mathrm{BG}}(T)\right)\right).
\end{aligned}
\tag{8}
$$

To obtain the frequency shift-induced phase change from T_{ref} to T, the respective reference phase at the reference temperature, T_{ref}, is subtracted from the even and odd echo at the current temperature, T, respectively.

$$
\begin{aligned}
\mathrm{cor}E_{\mathrm{even}} &= \left(\left|E_{\mathrm{even}}(T)\right|\right) \cdot \exp\left(\mathrm{i}\left(\phi_{e1} + 2\pi\Delta f_{\mathrm{PRF}}\tau + \Delta\varphi_{\mathrm{BG}}(T)\right)\right) \\
&\quad \cdot \exp\left(-\mathrm{i}\phi_{\mathrm{e1}}\right) = \left(\left|E_{\mathrm{even}}(T)\right|\right) \\
&\quad \cdot \exp\left(\mathrm{i}\left(2\pi\Delta f_{\mathrm{PRF}}\tau + \Delta\varphi_{\mathrm{BG}}(T)\right)\right) \\
\mathrm{cor}E_{\mathrm{odd}} &= \left(\left|E_{\mathrm{odd}}(T)\right|\right) \cdot \exp\left(\mathrm{i}\left(\phi_{o1} - 2\pi\Delta f_{\mathrm{PRF}}\tau + \Delta\varphi_{\mathrm{BG}}(T)\right)\right) \\
&\quad \cdot \exp\left(-\mathrm{i}\phi_{\mathrm{o1}}\right) = \left(\left|E_{\mathrm{odd}}(T)\right|\right) \\
&\quad \cdot \exp\left(-\mathrm{i}\left(2\pi\Delta f_{\mathrm{PRF}}\tau - \Delta\varphi_{\mathrm{BG}}(T)\right)\right).
\end{aligned}
\tag{9}
$$

Finally, we obtain a complex image that carries the PRFS phase by adding the complex conjugate of the reference-corrected odd echo to the reference-corrected even echo. This calculation removes the unknown rotational shift about the *z*-axis in the *x*–*y* plane and thus corrects for conductivity change-induced bias.

$$
\Delta\Phi_{\mathrm{FSE}} = \angle\left(\mathrm{cor}E_{\mathrm{even}} \cdot \mathrm{conj}(\mathrm{cor}E_{\mathrm{odd}})\right) = 4\pi\Delta f_{\mathrm{PRF}}\tau. \tag{10}
$$

With $2\pi\Delta f_{\mathrm{PRF}} = \alpha\gamma B_0 \Delta T$, we obtain:

$$
\Delta T = \frac{\Delta\Phi_{\mathrm{FSE}}}{2\alpha\gamma B_0 \tau}. \tag{11}
$$

This phase subtraction operation doubles the phase sensitivity. However, assuming the same noise level of both even and odd Echo image, the phase noise is also increased by a factor $\sqrt{2}$ due to the phase subtraction operation. Thus, the total TNR gain is $\sqrt{2}$.

$$
\mathrm{TNR}_{\mathrm{TFSE}} = \sqrt{2} \cdot \mathrm{TNR}_{E_{\mathrm{even/odd}}}. \tag{12}
$$

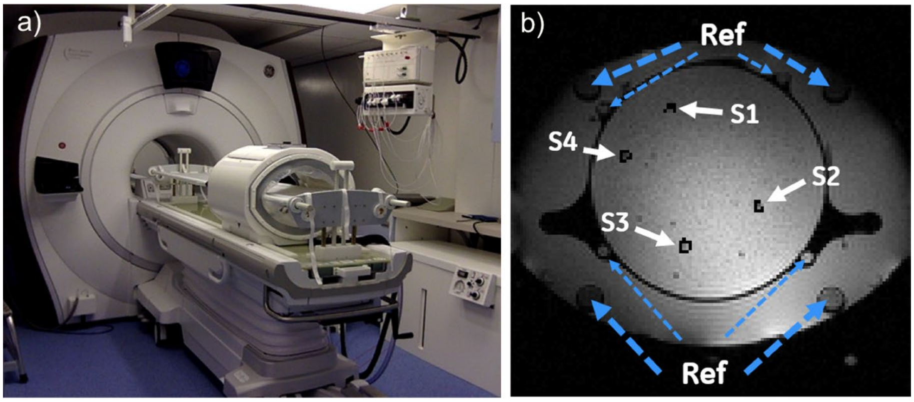

Fig. 2 **a** Hybrid system for MR-monitored RF mild HT consisting of a 1.5T MR scanner and an RF applicator for heating. The Bowman probes are mounted on a guide rail on the ceiling and the container for water cooling the patient via a bolus is visible on the bottom right of the image. **b** Axial magnitude image showing the cross-section of phantom heating setup. The larger outer four reference tubes containing silicone are placed on the outer edge of the applicator frame. Four additional smaller reference tubes filled with peanut oil are placed in between the phantom and the water bolus. S1 to S4 delineate the region of interest around the Bowman temperature sensor tip

Methods

A GE 1.5T Optima MR450w (Milwaukee, WI) in combination with a MR-compatible BSD-2000 Sigma Eye applicator (PYREXAR Medical, Salt Lake City, UT) is used for all scans (Fig. 2a). This RF heat applicator operates at 100 MHz simultaneously to the MRI. Coaxial filters are installed to prevent the 100 MHz signal from interfering with the MRI signal acquisition. Reconstruction, post processing, and image analysis were performed using MATLAB (MathWorks, Natick, MA). In total, four RF-immune thermistors with high-impedance carbon wires (‘Bowman’ temperature probes [30]) were used during the phantom heating experiments. Human subject scans at constant temperature were conducted.

DEGRE

A slice interleaved acquisition order for more efficient volume coverage is chosen (Fig. 1a). Within the TR of 620 ms, one phase encode step is measured for all 25 slices, with 24.8 ms per slice and line. For scanning 128 phase encode steps for all slices, the total scan time amounted to 83 s. Scan parameters for DEGRE: $TE_1 = 4.8$ ms, $TE_2 = 19.1$ ms, TR = 620 ms, matrix = 128 × 128, FOV = 50 cm × 50 cm, flip angle = 40°, number of slices = 25, slice thickness = 10 mm, bandwidth = 325.5 Hz/px.

TFSE

By placing two dual-band quadratic-phase RF pulses as saturation bands outside a field of view (FOV) of interest, the number of *k*-space lines to be acquired can be reduced, further accelerating the scan time [26]. The echo train length (ETL) corresponds to the number of echoes acquired within one shot. To limit the impact of oscillation artifacts [15, 24], the first two echoes were discarded as dummies. To reduce blurring and counterbalance signal loss with T2 decay with a higher number of ETL, the refocusing RF flip angles were increased towards the end of the ETL. The optimal amplitude modulation during the course of the echo train is deduced here [25, 31]. A centric acquisition order allows the filling of the *k*-space center with higher signal amplitude. Scan parameters for TFSE: matrix = 192 × 78, FOV = 50 cm × 30 cm, flip angle = 90°, number of slices = 25, slice thickness = 10 mm, bandwidth = 325.5 Hz/px, $\tau = 30$ ms, ETL per shot = 41, TR = 1.5 s, dummy ETL per shot = 2, echo spacing = 6.76 ms, scan time = 50 s.

For efficient volume coverage, a slice-interleaved acquisition scheme was used. For acquiring 78 phase steps with ETL = 39 (excluding two dummies), two shots were needed to acquire each, the CP and CPMG image. The hierarchy of the loops was implemented as follows: the outermost loop is the one over the two different groups of *k*-space lines. First the CPMG, then the CP image is acquired in alternating shots. Within the CPMG/CP loop, there is a loop through all slices, with 500 ms per slice. For each phase cycle, a period of 25 × 500 ms = 12.5 s was needed. Even though the minimal TR was set to 1.5 s, effective TR was therefore 12.5 s. The overall scan time for both shots and both phase cycles was 50 s. This acquisition scheme allows us to shorten the scan time by reducing the number of slices without compromising in SNR, since the effective TR for each slice is 12.5 s. For DEGRE, in contrast, shortening the TR of 620 ms by reducing the number of slices will decrease SNR because of the reduced time for T1 relaxation.

The even and odd echo signals initially oscillate around a smooth signal before reaching a pseudo-steady-state [25]. For areas with very low SNR, this would result in artifacts. Therefore, an oscillation-correction step was calculated [15, 24].

Phantom heating experiment

A cylindrical phantom 30 cm in diameter and 40 cm in depth was heated. The phantom consisted of demineralized water, ‘super stuff’ (TX-151), a hydrophilic organic polymer solidifying powder, and NaCl, which mimicked the electrical properties of human tissue. Several catheters passed through the phantom parallel to the cylinder’s axis, allowing for the insertion of temperature probes. To match the position of the sensor tip to the respective MR data, in total four Bowman probes were placed into the approximate middle of the phantom with the motorized positioning machine. After finishing the heating experiments, the actual inserted length of the Bowman probes was manually gauged to match it to the corresponding MR slice. This step was necessary because friction inside the catheters during the automatic insertion process caused a variation of the probe positions of up to 3 cm relative to each other.

After the acquisition of the baseline reference images at a scanner room temperature of 20 °C before heating, the BSD applicator was turned on at 400 W with phase settings to achieve a focus 3 cm below the center of the applicator. DEGRE and TFSE scans were alternated. RF power was turned on for 25 min during the experiment. To prove repeatability, the experiment was repeated twice with an interval between the experiments of more than 12 h to allow the phantom to cool down.

B_0 drift correction

The B_0 drift in both DEGRE and TFSE scans for the phantom heating experiment was corrected based on the signal of four larger integrated reference tubes filled with silicone inside the BSD applicator and four thinner additional reference tubes filled with peanut oil (‘Ref’ in Fig. 2b). The nonpolar structure of silicone (polysiloxane) makes the electron shielding of the hydrogen protons insensitive to temperature change. Since silicone has a very short T2 and T2* value, the signal has largely decayed in the long echo GRE ($TE_2 = 19.1$ ms) as well in the FSE image. Therefore, the phase signal for B_0 drift detection is only extracted from the short TE GRE image, referred to as TE_1. The phase difference signal between the images at reference temperature and current scan inside the reference tubes of the short echo time is purely due to B_0 drift. The resulting B_0 drift-induced temperature error was derived as follows:

$$\Delta T_{\text{error}} = \frac{\Delta\phi_{\Delta B_0}(\text{TE}_1)}{\alpha\gamma B_0 \text{TE}_1} = \frac{\phi(\text{TE}_1, T_{\text{ref}}) - \phi_{\Delta B_0}(\text{TE}_1, T)}{\alpha\gamma B_0 \text{TE}_1} = \frac{\angle\left(\exp\left(\mathrm{i}2\pi f \text{TE}_1\right)\cdot \operatorname{conj}\left(\exp\left(i2\pi\left(f + \Delta f_{\Delta B_0}\right)\text{TE}_1\right)\right)\right)}{\alpha\gamma B_0 \text{TE}_1}. \tag{13}$$

A polynomial function was fitted to the temperature error data inside these masked reference tubes to extract the current B_0 drift within the phantom. The B_0 drift-induced temperature change was fitted across all 25 slices to a polynomial function of first order with no constraint set in the time domain. This is achieved via matrix inversion corresponding to a linear regression algorithm in MATLAB [29]. Additional weighting for the fitting algorithm was realized by the magnitude data inside the reference tubes.

For the TFSE scans, the drift correction value was found by linear interpolation over time of the ΔT_{error} values.

In vivo leg scans

The current intention is to use the MR-compatible BSD-2000 Sigma EYE applicator for routine treatment of cancer in the pelvis. As sarcomas in the leg are less sensitive to motion, MR thermometry has a higher success rate with this setup [32–35]. Here we compared TFSE with DEGRE in three volunteers who were placed within the RF applicator and a filled water bolus without heat application. First, we waited 5–10 min to allow the water to stabilize and the muscles to relax before the acquisition of the reference scans. Compared to the scan parameters used for the phantom heating, we reduced the FOV in the phase-encode direction for TFSE further as follows: for volunteers #1 and #2: FOV = 50 cm × 25 cm, ETL = 34, matrix = 192 × 64, for volunteer #3: FOV = 50 cm × 20 cm, ETL = 28, matrix = 192 × 52. Other scan parameters, also for DEGRE, remained the same. The signal within the subcutaneous fat layer of the respective scan was used for B_0 drift correction. The masks were drawn manually for each slice (Fig. 6a–c) and a polynomial function of first order was fitted over the 3D volume comprising all 25 slices.

Experimental TNR efficiency

To measure the precision of both MR thermometry methods, a normalized TNR is calculated as the inverse of the standard deviation within a large ROI of the respective temperature increase maps before heating:

$$\text{TNR}(\Delta T) = \frac{1}{\text{std}(\Delta T)}. \tag{14}$$

The variation of ΔT within the considered ROI has no systematic variation in phase with position since the B_0 drift was corrected and no temperature change was induced.

For a just comparison of the resulting experimental TNR of both sequences, the effect of different scan parameters on SNR must be accounted for. Therefore, we speak of TNR efficiency (TNR_{eff}) and scale the measured and normalized TNR of TFSE with the square roots of the scan time and consider the difference in voxel size with a correction factor corr as follows:

$$\text{TNR(TFSE)}_{\text{eff}} = \text{corr}\cdot\text{TNR(TFSE)}_{\text{exp}} = \frac{\mathrm{d}V_{\text{DEGRE}}}{\mathrm{d}V_{\text{TFSE}}}\cdot\frac{\sqrt{t_{\text{DEGRE}}}}{\sqrt{t_{\text{TFSE}}}}\cdot\text{TNR(TFSE)}_{\text{exp}}, \tag{15}$$

where $\mathrm{d}V$ is the respective voxel size, t is the scan duration, and $\text{TNR(TFSE)}_{\text{exp}}$ is the measured TNR in the TFSE images. With $\text{TNR(TFSE)}_{\text{eff}}$ we obtain the TNR of the TFSE sequence corresponding to the TNR of the DEGRE sequence if voxel volume and acquisition time were the same. Using the values as specified above, we obtain corr = 1.96 for the phantom scanning, corr = 1.93 for volunteers #1 and #2, and corr = 1.96 for volunteer #3.

Results

Phantom heating experiment

All three heating experiments produced a recurrent heating pattern over time and in space. The correspondence of the B_0 drift-corrected MR temperature values to the probe data is shown in Fig. 4. The TFSE and DEGRE temperatures were calculated as the mean value within an ROI of 10–12 pixels around the four probe positions (Fig. 2b). The standard deviation of the TFSE data was scaled with the correction factor from Eq. 15. With a few exceptions, temperature values measured with TFSE corresponded well to the temperature probe data and the temperature increase curves acquired with DEGRE.

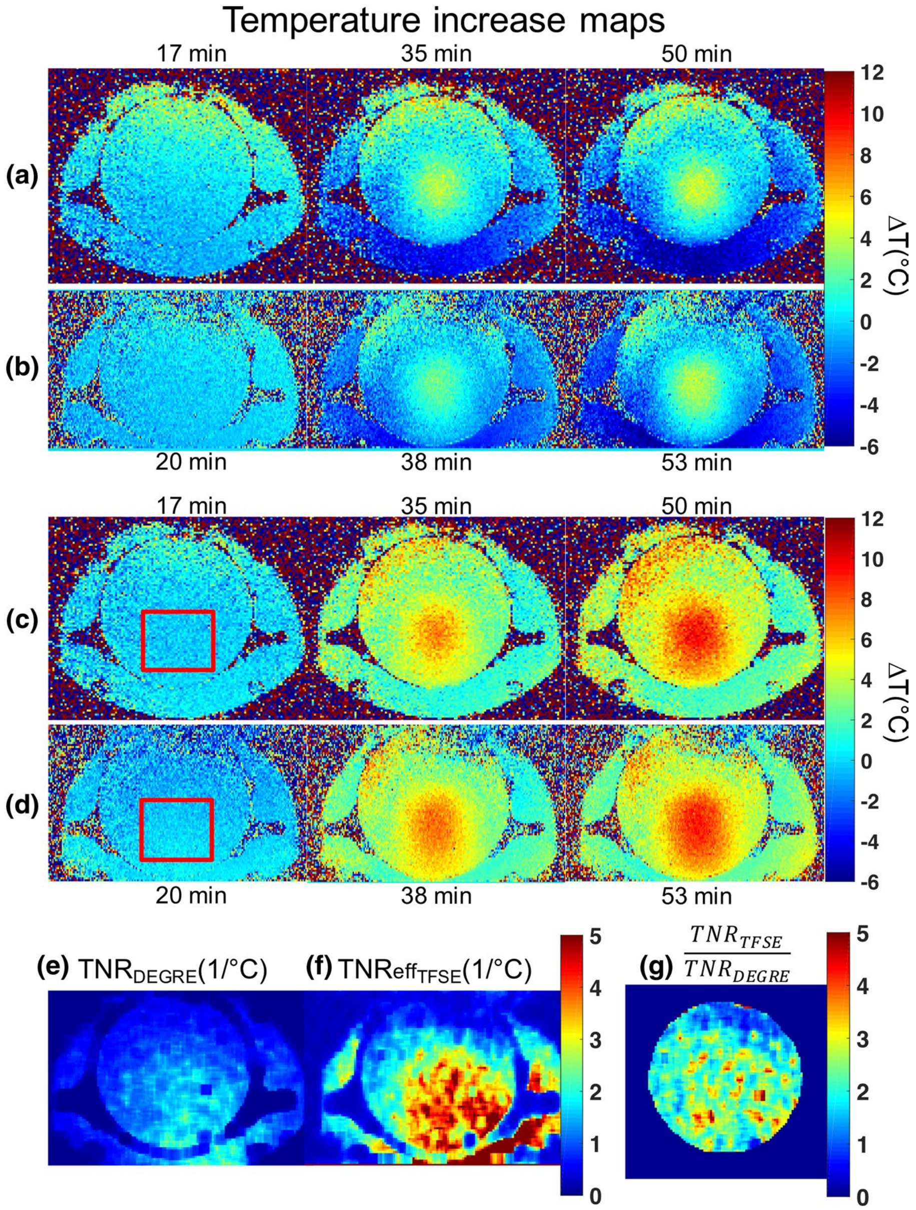

Fig. 3 Temperature change maps from DEGRE and TFSE images at 3 time points, respectively, after acquisition of a reference scan. The three time points correspond to the second, seventh and last data points of the heating experiment #1 in Fig. 4. The timings shown above and below the maps refer to the acquisition of the first DEGRE image and correspond to the time axis of Fig. 4. Red boxes indicate ROI used for TNR calculation. **a** DEGRE temperature maps before B_0 drift correction, **b** TFSE temperature maps before B_0 drift correction, **c** DEGRE temperature maps after B_0 drift correction, **d** TFSE temperature maps after B_0 drift correction, **e** TNR map of DEGRE temperature map, **f** TNR efficiency map of TFSE temperature map, that was scaled with the correction factor of 1.96, **g** ratio map of TFSE $\mathrm{TNR_{eff}}$ map in **f** divided by DEGRETNR map in **e** calculated as $\mathrm{Ratio} = \frac{\mathrm{TNR_{eff}(TFSE)}}{\mathrm{TNR_{DEGRE}}}$

The temperature change maps for both methods at three time points after acquisition of the first reference scan are shown in Fig. 3 as representative maps. The slice closest to all temperature probes was chosen. Figure 3a, b show the temperature maps before correcting for B_0 drift, and Fig. 3c, d the ones after drift correction. 17 min after the reference scan, before any heating was applied, significant overestimation of temperature in the upper part of the image was observed due to the B_0 drift. The B_0 drift caused a bias in the temperature maps of about 8 °C inside 50 min prior to drift correction.

The first ΔT maps of the first experiment before heating were used to compare the TNR performance [36]. Within the large ROI delineated by the red boxes in Fig. 3c, d, 0.26 ± 0.69 °C was calculated for the DEGRE map and 0.27 ± 0.63 °C was obtained for the TFSE map. When considering the correction factor described in Eq. 15, we obtain a TNR efficiency ratio of $\frac{\mathrm{corr \cdot TNR(TFSE)_{exp}}}{\mathrm{TNR(DEGRE)_{exp}}} = 2.15$.

To illustrate altering phase precision in space, TNR maps of both TFSE and DEGRE temperature maps are generated by considering a neighborhood of 5×5 pixels (Fig. 3e, f)—again using the ΔT maps before heating and after drift correction. To obtain the $\mathrm{TNR_{eff}}$ map for TFSE, the initial TNR map was multiplied by the correction factor of 1.96. Both methods showed higher $\mathrm{TNR_{eff}}$ in the bottom right part, which corresponds to the area with a higher SNR (Fig. 2b). The $\mathrm{TNR_{eff}}$ comparison ratio-map in Fig. 3g was generated with the formula: $\mathrm{Ratio} = \frac{\mathrm{TNR_{TFSE}}}{\mathrm{TNR_{DEGRE}}}$.

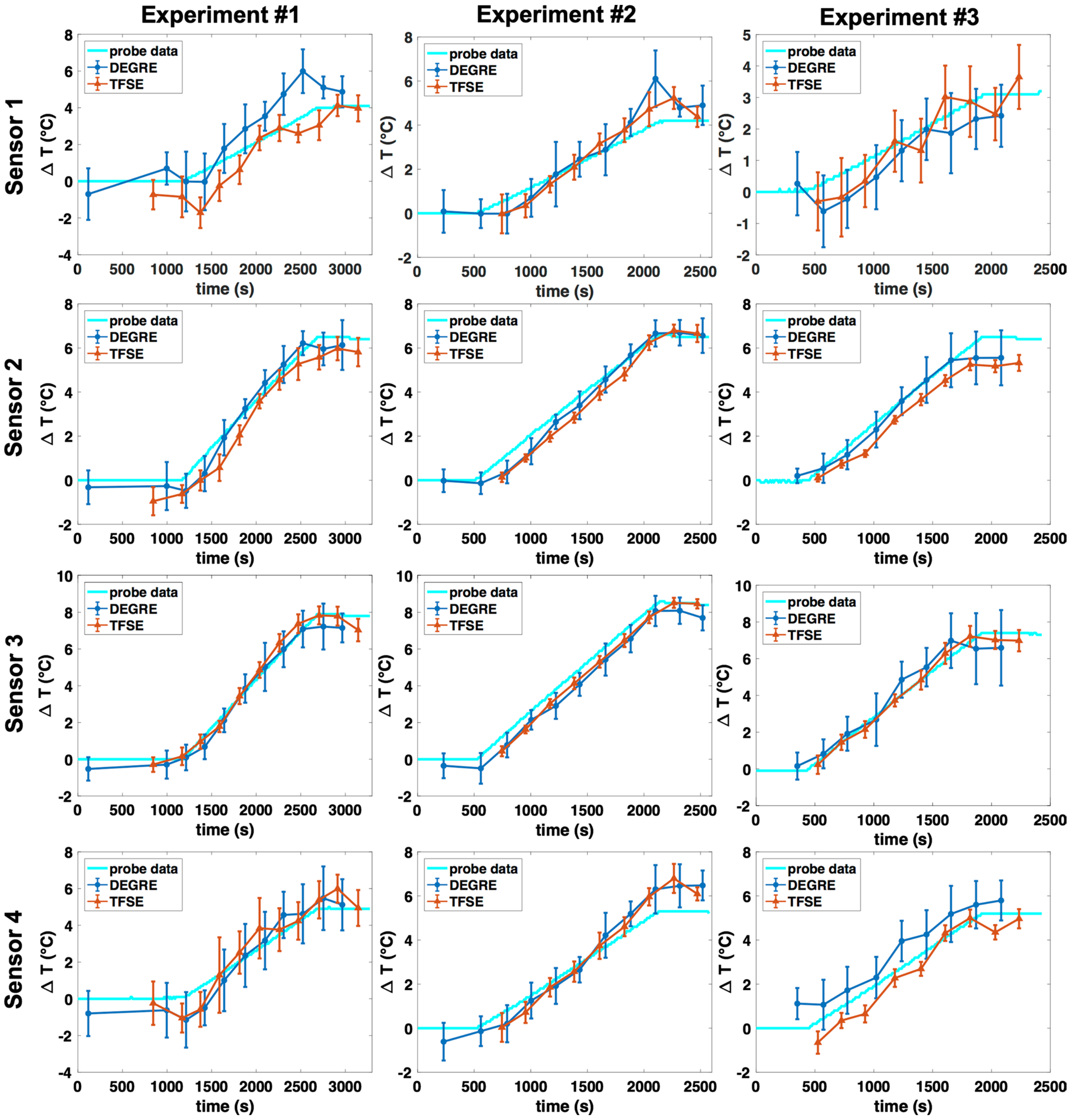

Fig. 4 Mean temperature change values in small ROIs for TFSE and DEGRE method and temperature probe data of sensor located within ROI shown as a function of time. The respective ROIs are drawn in Fig. 2b. Each column represents one independent heating experiment

Bland–Altman plots

For the phantom-heating dataset, the relations between the respective MR temperature measurement technique (as shown in Fig. 4) and the Bowman probe measurements are plotted in two Bland–Altman plots, which are overlaid in one figure (Fig. 5). The difference between the averaged ΔT value within a region of interest (ROI) around a temperature probe in the respective MR temperature maps and the ΔT value recorded with the Bowman probe is plotted against the average of both values. The TFSE method showed a lower standard deviation. The deviation of − 0.11 °C for the mean difference over all averaged measurement points for DEGRE and of − 0.36 °C for TFSE suggest a larger bias for

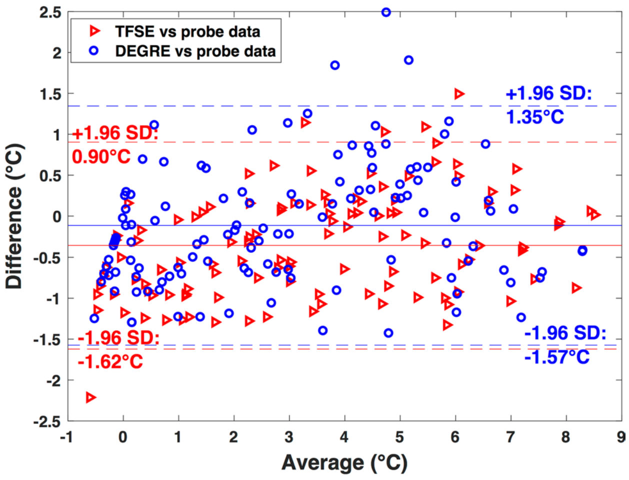

Fig. 5 Bland–Altman plots: mean values of ROI in TFSE and DEGRE Δ*T* maps vs. corresponding Bowman temperature probe value as ground truth. Data points from all three phantom heating experiments, as plotted in Fig. 4, are considered

TFSE. However, this bias is still low compared to the potential bias that may originate from positioning uncertainties. Even though we estimate our probe positioning accuracy to be within 1 voxel, the maximum measured temperature gradient of 2–3 °C across 3 voxels allows for experimental uncertainties.

In vivo leg scans

A representative axial slice of the thighs delineates the regions used for B_0-drift correction and the chosen ROI for illustrating the effect of the drift on both methods (Fig. 6). Inside 25 min, a B_0-drift of 0.06 ppm caused a temperature error of 6 °C in the ROI delineated by the white arrow in Fig. 6a. Using the subcutaneous fat for drift correction could reduce the error to less than 1 °C for both methods.

We observed that the TFSE temperature maps were noisier in the anterior part of the image in comparison to the DEGRE method (Fig. 6g–i. This reflects the lower T2*

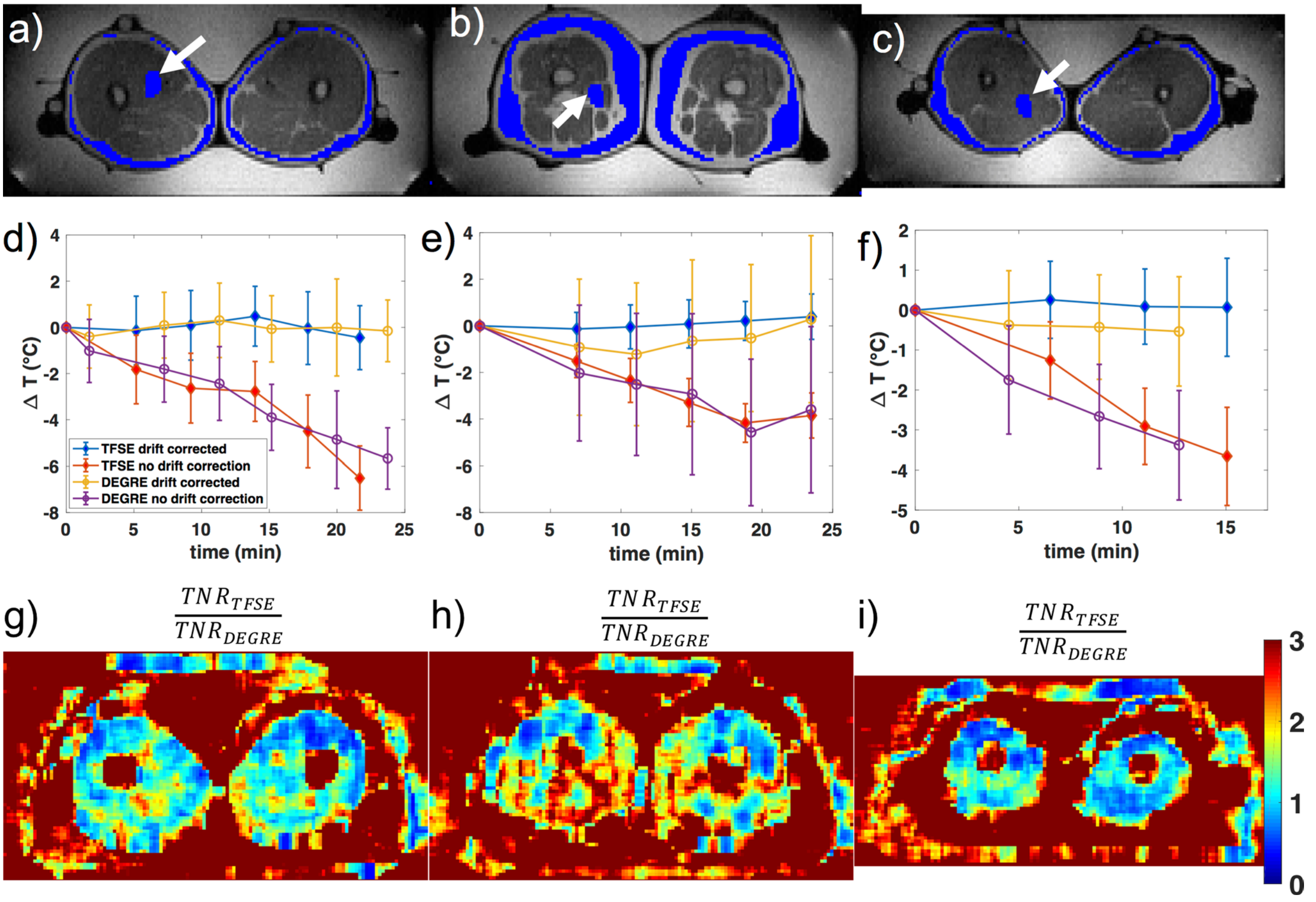

Fig. 6 Effect of B_0 drift on TFSE and DEGRE data in the upper leg at constant temperature. **a**–**c** Gray scale axial images (TFSE images without delay ($\tau = 0$ ms)). The blue mask within the subcutaneous fat layer shows the manually selected area for B_0 drift correction in the representative slice. The white arrows point at a blue ROI within muscle tissue, for which the mean and standard deviation values of the TFSE and DEGRE temperature change maps over time are compared in the graphs below (**d**–**f**). Representative ratio maps for the respective above subjects are shown in (**g**–**i**), calculated as: Ratio = $\frac{\mathrm{TNR_{eff}(TFSE)}}{\mathrm{TNR_{DEGRE}}}$

in the anterior part of the image due to B_0-inhomogeneity. Nevertheless, we achieved an overall $\mathrm{TNR}_{\mathrm{eff}}$ improvement by a factor of 1.37 ± 0.67, 1.27 ± 0.44 and 1.20 ± 0.77 for subject a, b, and c of Fig. 6, respectively, if we consider areas with $\mathrm{TNR}_{\mathrm{eff}} > 0.6$ for calculating the ratio between both $\mathrm{TNR}_{\mathrm{eff}}$ maps.

Discussion

The B_0-drift correction for the phantom heating experiment was based on the short TE signal of the DEGRE inside built-in silicon tubes of the BSD applicator. The temporal interpolation method of the B_0-drift maps for drift correction of TFSE data assumed negligible B_0-drift between the first DEGRE and the first TFSE reference scan. This has added a locally varying, but temporally constant offset to the TFSE temperature maps dependent on the B_0-drift between the reference scans of DEGRE and TFSE, as observed for the data around sensor 2 in Fig. 4. To make B_0-drift correction for TFSE independent of additional GRE-images, alternative reference tubes with longer T2, for example oil, must be added. For in vivo scans, proper subcutaneous fat layers can be used.

Fewer switching of imaging gradients during TFSE scans compared to DEGRE could lead to lower acoustic noise. The different use of imaging and crushing gradients in both sequences could potentially cause a more advantageous or disadvantageous B_0-drift behavior due to hardware heating. Both effects need to be investigated quantitatively. However, the typical concern of a high specific absorption rate in patients during FSE is rendered obsolete in the context of mild HT.

The scan time is reduced by suppressing the signal from the surrounding water bolus during TFSE, but the method also becomes insensitive to potential flow artifacts originating from the suppressed area. On the other hand, a non-perfect suppression, and therefore folding of signal outside the FOV, might have caused the signal dropout seen in Fig. 3f).

The sequence parameters for the standardized DEGRE sequence were optimized with regard to the volume coverage constraints. Given both TEs, 620 ms was the shortest possible TR for covering 25 slices. For a known T1 value, the flip angle can then be chosen using the Ernst equation. To further improve SNR for the DEGRE sequence, the readout bandwidth could be decreased. However, special care must be taken with regards to image distortion artifacts in case of an inhomogeneous field when decreasing the readout bandwidth. Another approach while maintaining a high bandwidth is to acquire the same line of *k*-space multiple times in the same time as once at low bandwidth. These echoes would be then combined using a weighting that gives an optimal TNR.

For optimal phase-to-noise ratio, thus TNR, TE must be equal to $\mathrm{T2}^*$ in the case of GRE and τ must be equal to $\mathrm{T2}^*$ in case of TFSE [37]. The lower TNR improvement factor for the in vivo experiments suggests that the waiting time τ needs to be adjusted to shorter $\mathrm{T2}^*$. TFSE has the advantage over DEGRE that τ can be chosen as $\mathrm{T2}^*$ for both CP and CPMG acquisition, whereas the DEGRE approach always requires two different TEs for correction of conductivity effects. If TE is increased to adjust for a longer $\mathrm{T2}^*$, the total scan time of DEGRE would increase by this time difference multiplied by the number of slices and the number of phase-encode steps. In contrast, the increase in scan time by increasing τ for TFSE is insignificant. For tissues with very short T2, it becomes necessary to reduce the ETL during TFSE, leading to an increased number of shots and thus a decrease in TNR efficiency.

Both DEGRE and TFSE are sensitive to B_1 inhomogeneity. In case of DEGRE, the Ernst angle will not be achieved. In case of TFSE, a deviation from the optimal train of refocusing pulse flip angles will be missed. Furthermore, differences in the measured slice profile and slice thickness between both methods may occur.

In comparison to DEGRE, TFSE scan time can be potentially reduced further for monitoring a more localized heating by reducing the number of slices without compromising in TNR. Quantitative evaluation of the phantom measurement data suggests that TFSE can potentially improve temperature precision, as TNR efficiency more than doubled for the given imaging parameters. Yet, these findings are the result of the chosen parameters and experimental setting. Further optimization of both sequences for another application may lead to different results.

Further investigation would include studying how the RF applicator may affect the TNR performance of both sequences differently [38].

Conclusions

A novel thermally sensitive FSE sequence has been examined for monitoring mild RF-HT. Using phase-cycling, the echoes are split and the confounding effect of temperature-dependent tissue conductivity on phase is corrected for. This constitutes a major advantage compared to other echo splitting methods for FSE-based PRFS measurements without phase-cycling.

The reduced scan time of TFSE in comparison to DEGRE is clinically very relevant: patient comfort can be increased, intra-scan motion can be avoided, or additional interventional MR scans for tumor characterization can be added instead.

Acknowledgements This project was funded by the European Commission under Grant Agreement Number 605162. Research support was received from GE Global Research. The authors would like to thank Abdelali Ameziane for technical support and Fatih Süleyman Hafalir for helpful discussions.

Author's contribution Wu, Mulder, Zur and Menzel contributed to the design of the study. Conceptual work on the method was performed by Zur and Wu. Wu and Mulder performed the measurements and acquired the data. The analysis and interpretation of data was done by Wu and Zur. Wu drafted the manuscript. Mulder, Zur, Lechner-Greite, Menzel, Paulides, van Rhoon and Haase were involved in critical revision of the manuscript.

Compliance with ethical standards

Conflict of interest Yual Zur, Silke Lechner-Greite, and Marion Menzel were employed with GE Healthcare during the generation of the presented work. The remaining authors have no conflict of interest to declare.

Ethical standards For the in vivo feasibility study, three healthy subjects were scanned with approval by the Erasmus Medical Center Ethics Review Board (METC 2005-340).

Informed consent Informed written consent was obtained from each volunteer prior to the study.

References

1. Kampinga HH (2006) Cell biological effects of hyperthermia alone or combined with radiation or drugs: a short introduction to newcomers in the field. Int J Hyperth 22(3):pp. 191–196
2. Wust P, Gellermann J, Harder C, Tilly W, Rau B, Dinges S, Schlag P, Budach V, Felix R (1998) Rationale for using invasive thermometry for regional hyperthermia of pelvic tumors. Int J Radiat Oncol Biol Phys 41(5):pp. 1129–1137
3. van der Zee J, Peer-Valstar JN, Rietveld PJ, de Graaf-Strukowska L, van Rhoon GC (1998) Practical limitations of interstitial thermometry during deep hyperthermia. Int J Radiat Oncol Biol Phys 40(5):pp. 1205–1212
4. Gellermann J, Wlodarczyk W, Ganter H, Nadobny J, Fähling H, Seebass M, Felix R, Wust P (2005) A practical approach to thermography in a hyperthermia/magnetic resonance hybrid system: validation in a heterogeneous phantom. Int J Radiat Oncol Biol Phys 61(1):pp. 267–277
5. McDannold N (2005) Quantitative MRI-based temperature mapping based on the proton resonant frequency shift: review of validation studies. Int J Hyperth 21(6):pp. 533–546
6. Ishihara Y, Calderon A, Watanabe H, Okamoto K, Suzuki Y, Kuroda K, Suzuki Y (1995) A precise and fast temperature mapping using water proton chemical shift. Magn Reson Med 34(6):pp. 814–823
7. Gellermann J, Wlodarczyk W, Hildebrandt B, Ganter H, Nicolau A, Rau B, Tilly W, Fähling H, Nadobny J, Felix R, Wust P (2005) Noninvasive magnetic resonance thermography of recurrent rectal carcinoma in a 1.5 tesla hybrid system. Cancer Res 65(13):pp. 5872–5880
8. Gellermann J, Hildebrandt B, Issels R, Ganter H, Wlodarczyk W, Budach V, Felix R, Tunn PU, Reichardt P, Wust P (2006) Noninvasive magnetic resonance thermography of soft tissue sarcomas during regional hyperthermia. Cancer 107(6):pp. 1373–1382
9. Peters RD, Henkelman RM (2000) Proton-resonance frequency shift MR thermometry is affected by changes in the electrical conductivity of tissue. Magn Reson Med 43(1):pp. 62–71
10. Paulides MM, Curto S, Wu M, Winter L, van Rhoon GC, Yeo DTB (2017) Advances in magnetic resonance guided radiofrequency hyperthermia. In: 11th European Conference on Antennas and Propagation, Paris, pp. 3692–3696. https://doi.org/10.23919/eucap.2017.7928684
11. Vlaardingerbroek MT, Boer JA (2003) Magnetic resonance imaging. Springer, Berlin. https://doi.org/10.1007/978-3-662-05252-5
12. Edelstein WA, Glover GH, Hardy CJ, Redington RW (1986) The intrinsic signal-to-noise ratio in NMR imaging. Magn Reson Med 3(4):pp. 604–618
13. Ronnau J, Haimov S, Gogineni S (1994) The effect of signal-to-noise ratio on phase measurements with polarimetric radars. Remote Sens Rev 9(1–2):pp. 27–37
14. Winter L, Oberacker E, Paul K, Ji Y, Oezerdem C, Ghadjar P, Thieme A, Budach V, Wust P, Niendorf T (2016) Magnetic resonance thermometry: methodology, pitfalls and practical solutions. Int J Hyperth 32(1):63–75
15. Zur Y (2015) A new time shifted fast spin echo thermometry sequence. In: Proceedings of the 23rd scientific meeting, International Society for Magnetic Resonance in Medicine, Toronto, p 4054
16. Vogel MW, Pattynama PM, Lethimonnier FL, Le Roux P (2003) Use of fast spin echo for phase shift magnetic resonance thermometry. J Magn Reson Imaging 18(4):507–512
17. Splice Schick F (1997) Sub-second diffusion-sensitive MR imaging using a modified fast spin-echo acquisition mode. Magn Reson Med 38(4):pp. 638–644
18. Paysen H, Paul K, Pham M, Winter L, Niendorf T (2017) Toward hybrid MR thermometry in aqueous and adipose tissue using simultaneous dual contrast weighting with double echo rare imaging. In: Proceedings of the 25th scientific meeting, International Society for Magnetic Resonance in Medicine, Honolulu, p 1181
19. Norris DG (2007) Selective parity rare imaging. Magn Reson Med 58(4):643–649
20. Zur Y, Stokar S (1987) A phase-cycling technique for canceling spurious echoes in NMR imaging. J Magn Reson 71(2):212–228. https://doi.org/10.1016/0022-2364(87)90051-5
21. Carr HY, Purcell EM (1954) Effects of diffusion on free precession in nuclear magnetic resonance experiments. Phys Rev 94(3):630–638
22. Meiboom S, Gill D (1958) Modified spin-echo method for measuring nuclear relaxation times. Rev Sci Instrum 29(8):688–691
23. Norris DG, Bornert P (1993) Coherence and interference in ultrafast RARE experiments. J Magn Reson A 105(2):123–127
24. Zur Y, Chen W (2014) A technique to eliminate artifacts in 3D fast spin echo imaging. In: Proceedings of the 22nd scientific meeting, International Society for Magnetic Resonance in Medicine, Milan, p 1648
25. Zur Y (2017) Analysis of the multi-echo spin-echo pulse sequence. Concepts Magn Reson A 46A:e21402. https://doi.org/10.1002/cmr.a.21402
26. Zur Y (2016) Improved thermometry based on a fast spin echo sequence. In: Proceedings of the 24th scientific meeting, International Society for Magnetic Resonance in Medicine, Singapore, p 3598
27. El-Sharkawy AM, Schär M, Bottomley PA, Atalar E (2006) Monitoring and correcting spatio-temporal variations of the MR scanner's static magnetic field. Magn Reson Mater Phy 19(5):223–236
28. Bing C, Staruch RM, Tillander M, Köhler MO, Mougenot C, Ylihautala M, Laetsch TW, Chopra R (2016) Drift correction for accurate PRF-shift MR thermometry during mild hyperthermia treatments with MR-HIFU. Int J Hyperth 32(6):pp. 673–687

29. Hofstetter LW, Yeo DT, Dixon WT, Kempf JG, Davis CE, Foo TK (2012) Fat-referenced MR thermometry in the breast and prostate using IDEAL. J Magn Reson Imaging 36(3):722–732
30. Bowman RR (1976) A probe for measuring temperature in radio-frequency-heated material. IEEE Trans Microw Theory Tech 24(1):43–45
31. Busse RF, Brau AC, Vu A, Michelich CR, Bayram E, Kijowski R, Reeder SB, Rowley HA (2008) Effects of refocusing flip angle modulation and view ordering in 3D fast spin echo. Magn Reson Med 60(3):640–649
32. Craciunescu OI, Stauffer PR, Soher BJ, Wyatt CR, Arabe O, Maccarini R, Das SK, Cheng KS, Wong TZ, Jones EL, Dewhirst MW, Vujaskovic Z, MacFall JR (2009) Accuracy of real time noninvasive temperature measurements using magnetic resonance thermal imaging in patients treated for high grade extremity soft tissue sarcomas. Med Phys 36(11):4848–4858
33. Simonis FFJ, Petersen ET, Lagendijk JJW, van den Berg CAT (2016) Feasibility of measuring thermoregulation during RF heating of the human calf muscle using MR based methods. Magn Reson Med 75:1743–1751
34. Simonis FFJ, Raajimakers AJE, Lagendijk JJW, van den Berg CAT (2017) Validating subject-specific RF and thermal simulations in the calf muscle using MR-based temperature measurements. Magn Reson Med 77:1691–1700
35. Dadakova T, Gellermann J, Voigt O, Korvink JG, Pavlina JM, Hennig J, Bock M (2015) Fast PRF-based MR thermometry using double-echo EPI: in vivo comparison in a clinical hyperthermia setting. Magn Reson Mater Phy 28:305–314
36. Marx M, Butts Pauly K (2016) Improved MRI thermometry with multiple-echo spirals. Magn Reson Med 76:747–756. https://doi.org/10.1002/mrm.25914
37. Yuan J, Mei CS, Panych LP, McDannold NJ, Madore B (2012) Towards fast and accurate temperature mapping with proton resonance frequency-based MR thermometry. Quant Imaging Med Surg 2(1):21
38. Gellermann J, Faehling H, Mielec M, Cho CH, Budach V, Wust P (2008) Image artifacts during MRT hybrid hyperthermia—causes and elimination. Int J Hyperthermia 24(4):327–335